Journal of Alloys and Compounds 801 (2019) 234–238

Contents lists available at ScienceDirect

Journal of Alloys and Compounds

journal homepage: http://www.elsevier.com/locate/jalcom

Mg_2Si-based thermoelectric compounds with enhanced fracture toughness by introduction of dual nanoinclusions

Gwansik Kim [a], Hyun Jun Rim [a], Hwijong Lee [a], Jeongmin Kim [a], Jong Wook Roh [b], Kyu Hyoung Lee [a, **], Wooyoung Lee [a, *]

[a] Department of Materials Science and Engineering, Yonsei University, Seoul, 03722, Republic of Korea
[b] School of Nano & Materials Science and Engineering, Kyungpook National University, Sangju, 37224, Republic of Korea

ARTICLE INFO

Article history:
Received 12 March 2019
Received in revised form
21 May 2019
Accepted 6 June 2019
Available online 7 June 2019

Keywords:
Dual nanoinclusions
Reduced graphene oxides
Metal nanoparticles
Mg_2Si
Fracture toughness

ABSTRACT

Dual nanoinclusions of reduced graphene oxides (rGOs) and metal nanoparticles (NPs) were introduced into Al and Bi co-doped Mg_2Si thermoelectric (TE) compounds to enhance their fracture toughness (~0.82 MPa $m^{1/2}$ for pristine $Mg_{1.96}Al_{0.04}Si_{0.97}Bi_{0.03}$). The TE performance of $Mg_{1.96}Al_{0.04}Si_{0.97}Bi_{0.03}$ decreased by the introduction of nanoscale inclusions, mainly owing to the deterioration of the electronic transport properties originated from increased electron scattering. However, a significantly enhanced fracture toughness of 2.26 MPa $m^{1/2}$ was achieved by the introduction of 3 vol% rGOs (~5 nm thick and ~3 μm wide) and 0.6 vol% Sn NPs (50–150 nm), owing to the simultaneous activation of three different inhibition mechanisms for crack propagation: bridging of cracks, sheet pullout within the crack, and deflection of crack propagation.

1. Introduction

Silicide-based thermoelectric (TE) compounds (*n*-type Mg_2Si-based and *p*-type higher manganese silicide (HMS)-based alloys) are particularly promising materials for power generation applications at high temperatures, owing to their superior chemical and thermal stability compared with those of alloy-based TE materials (PbTe- and skutterudite-based compounds) [1,2]. Furthermore, silicide-based TE materials are composed of environment-friendly and naturally abundant elements. Among them, *n*-type Mg_2Si-based compounds have received a great amount of attention for automotive TE generators (ATEGs), owing to their high dimensionless TE figure of merit (*ZT*), low density (~1.99 g cm^{-3}), and low material cost (~$151/kg) [3]. *ZT* is calculated as $ZT = S^2 \cdot \sigma \cdot T/\kappa_{tot}$, where *S*, σ, κ_{tot}, and *T* represent the Seebeck coefficient, electrical conductivity, total thermal conductivity, and absolute temperature, respectively.

A high *ZT* value of ~1.2 at 700 K was obtained by the doping of Sn at the Si-site, mainly benefiting from an enhanced power factor (PF, $S^2 \cdot \sigma$) by enabling band convergence [4]. However, Sn-doped Mg_2Si cannot be used for high-temperature applications owing to the decomposition problem at ~773 K [5]. To address this problem, several compositional tuning approaches have been carried out and durable *ZT* values of ~0.55 at 720 K and ~0.82 at 873 K were obtained for Bi-doped Mg_2Si and Al and Bi co-doped Mg_2Si polycrystalline bulk, which were fabricated using a solid state reaction (SSR) and spark plasma sintering (SPS) [6–8].

Despite the durable TE performance of Al and Bi co-doped Mg_2Si at high temperatures, it suffers from poor mechanical reliability, particularly in the mechanically harsh environments of ATEGs. The fracture toughness (K_{Ic}) of $Mg_{1.96}Al_{0.04}Si_{0.97}Bi_{0.03}$ is limited to about 0.82 MPa $m^{1/2}$, which is significantly lower than that of its *p*-type counterparts such as HMS (K_{Ic} ~1.63 MPa $m^{1/2}$), even in a highly dense (>97% relative density) polycrystalline bulk [9,10]. To overcome this drawback, we fabricated two types of nanocomposites, $Mg_{1.96}Al_{0.04}Si_{0.97}Bi_{0.03}$ with reduced graphene oxides (rGOs) [11] and $Mg_{1.96}Al_{0.04}Si_{0.97}Bi_{0.03}$ with metal nanoparticles (NPs) [10], and achieved an improvement in K_{Ic} for both. Interestingly, we found that the inhibition mechanisms for crack propagation were different in the presence of rGOs (2-dimensional (2D) nanoinclusions) and metal NPs (3-dimensional (3D) nanoinclusions). Herein, we propose an advanced concept of TE nanocomposites for

* Corresponding author.
** Corresponding author.
E-mail addresses: khlee2018@yonsei.ac.kr (K.H. Lee), wooyoung@yonsei.ac.kr (W. Lee).

https://doi.org/10.1016/j.jallcom.2019.06.075
0925-8388/

enhanced mechanical reliability, in which multidimensional dual nanoinclusions (2D rGOs and 3D metal NPs) are introduced to maximize K_{Ic}, and demonstrate an experimental verification of our concept.

Bulk nanocomposites of $Mg_{1.96}Al_{0.04}Si_{0.97}Bi_{0.03}$ with dual nanoinclusions of few-layered rGOs (~5 nm thick and ~3 μm wide) and metal NPs (50–150 nm) were prepared. Although the maximum ZT of the nanocomposites were reduced to about 0.57 at 873 K owing to a decrease in PF and an increase in bipolar thermal conduction, the K_{Ic} greatly improved (~2.26 MPa $m^{1/2}$) owing to the simultaneous activation of three different crack propagation inhibition mechanisms: bridging of cracks, sheet pullout within the crack, and deflection of crack propagation.

2. Experimental

Al and Bi co-doped Mg_2Si ($Mg_{1.96}Al_{0.04}Si_{0.97}Bi_{0.03}$) powders were synthesized using the up-scaled SSR technique. The details of the process are described in our previous reports [7,8]. Hybrid powders of $Mg_{1.96}Al_{0.04}Si_{0.97}Bi_{0.03}$ with few-layered rGOs and metal NPs were prepared using an ultrasonics-based wet pulverizing-mixing process using a bar-type sonication system (Q700 Sonicator) and a subsequent mix-and-heat process. Firstly, $Mg_{1.96}Al_{0.04}Si_{0.97}Bi_{0.03}$ powders and rGOs were mixed in an n-hexane solution for 1 h to improve the dispersibility of the rGOs, and dried at 473 K for 30 h under air. Then, the mixtures of $Mg_{1.96}Al_{0.04}Si_{0.97}Bi_{0.03}$ powders with few-layered rGOs and metal acetates (copper(II) acetate ($(CH_3COO)_2Cu$), aluminum acetate ($(CH_3COO)_2(OH)Al$), and stannous acetate ($(CH_3COO)_2Sn$)) were prepared by high-energy ball milling (8000D, SPEX, USA) for 5 min. Finally, these mixtures were heat-treated at 473 K for 3 h (for the mixture with $(CH_3COO)_2Sn$) and at 573 K for 2 h (for the mixtures with $(CH_3COO)_2Cu$ and $(CH_3COO)_2(OH)Al$) under a mixed-gas condition with 95% N_2 and 5% H_2 to remove the acetate (−CH_3COO−).

Compacted bulks were prepared by SPS at 1023 K and 70 MPa for 5 min under a dynamic vacuum condition. The temperature dependences of σ and S were evaluated by a TE properties measurement equipment (ZEM-3, ULVAC, Japan) in the temperature range of 300–873 K. The Hall effect was measured in the van der Pauw configuration under a 1 T magnetic field, and the carrier concentration (n_c) and Hall mobility (μ_{Hall}) were estimated using a one-band model at 300 K. The total thermal conductivity (κ_{tot}) as a function of the temperature was calculated using the equation $\kappa_{tot} = \rho_s \cdot C_p \cdot \lambda$, where ρ_s is the density, C_p is the specific heat capacity, and λ is the thermal diffusivity. The temperature dependences of λ and C_p were measured using the laser flash method (Netzsch LFA-457, Germany) and differential scanning calorimetry (DSC 8000, Perkin Elmer, USA), respectively, under vacuum conditions.

K_{Ic} was calculated using the equation:

$$K_{Ic} = \chi\left(\frac{E}{H}\right)^{1/2}\frac{P}{a^{3/2}},$$

where P, E, H, and a are the applied load, Young's modulus, Vickers hardness, and radial crack length measured from the center of the indent, respectively, and χ is the calibration constant, with a value of 0.016 ± 0.004 [12]. H and a were measured using a Vickers hardness tester (HM-101, Mitutoyo, Japan) under a load of 2.942 N for a dwell time of 10 s.

3. Results and discussion

In the previous studies, we prepared two types of Mg_2Si-based nanocomposites ($Mg_{1.96}Al_{0.04}Si_{0.97}Bi_{0.03}$ with rGOs and $Mg_{1.96}Al_{0.04}Si_{0.97}Bi_{0.03}$ with metal NPs (Cu, Al, Sn)), expecting the crack propagation inhibition effect in the presence of nanoinclusions with high mechanical properties [10,11,13]. Improved K_{Ic} values were obtained for both rGO- and metal-NP-embedded $Mg_{1.96}Al_{0.04}Si_{0.97}Bi_{0.03}$, as shown in Fig. 1. Based on an investigation of their toughening behaviors, we concluded that the mechanisms for crack propagation inhibition were different for these nanocomposites. Evidences for three different mechanisms (bridging of cracks, sheet pullout within the crack, and deflection of crack propagation) were obtained for the 2D rGO-embedded nanocomposites [11], whereas only deflection of crack propagation was observed in the 3D metal-NP-embedded nanocomposites [10,13]. These results suggested that the introduction of dual nanoinclusions (2D rGOs and 3D metal NPs) would be an effective way to maximize K_{Ic}.

The SEM images in the insets of Fig. 1 show the introduced dual nanoinclusions of few-layered rGOs and metal NPs in $Mg_{1.96}Al_{0.04}Si_{0.97}Bi_{0.03}$ powders. As shown in Fig. 1, greatly enhanced K_{Ic} values (ranging from 2.07 to 2.32 MPa $m^{1/2}$), higher than that of p-type HMS (~1.63 MPa $m^{1/2}$), were obtained for the bulk materials (nanocomposites with dual nanoinclusions). To clarify the effect of the dual nanoinclusions on K_{Ic}, a microhardness tester was used to form radial cracks from the corners of the indentations. A microhardness indentation image of the nanocomposite with 3 vol% rGOs and 0.6 vol% Sn NPs is presented in Fig. S1. Fig. 2 shows the three different K_{Ic} enhancement mechanisms, indicating that our strategy of introducing multidimensional dual nanoinclusions is effective to maximize K_{Ic}. The exhibition of 2D rGOs at the grain boundaries mainly led to the mechanisms of the bridging of cracks (Fig. 2(a) and (b)) and sheet pullout within the cracks (Fig. 2(c) and (d)). The 3D metal NPs mainly activated the strengthening mechanism of the deflection of crack propagation, as shown in Fig. 2(e) and (f). Consequently, the K_{Ic} values of the nanocomposites with dual nanoinclusions were higher than those of the nanocomposites with single nanoinclusions, owing to the simultaneous activation of three toughening mechanisms.

We also investigated the change in the TE transport properties by the introduction of dual nanoinclusions. As shown in Fig. 3, we measured the electronic transport properties (S, σ) and calculated the PF. The properties of the metal-NP-embedded nanocomposites

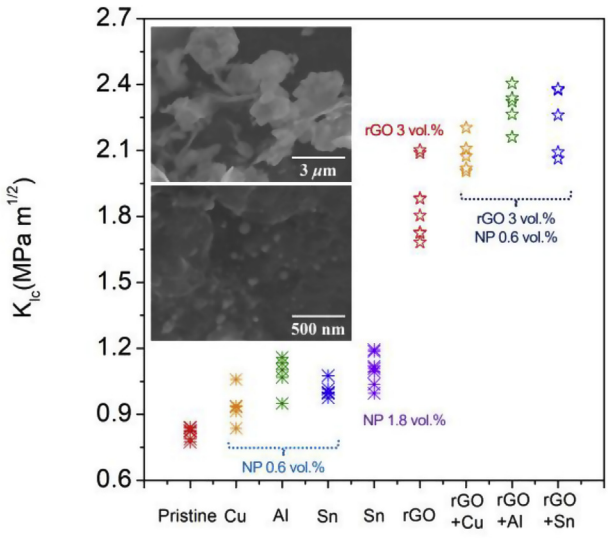

Fig. 1. K_{Ic} values of various nanocomposites. The insets show the SEM images of the introduced nanoinclusions of few-layered rGOs and metal NPs in $Mg_{1.96}Al_{0.04}Si_{0.97}Bi_{0.03}$ powder.

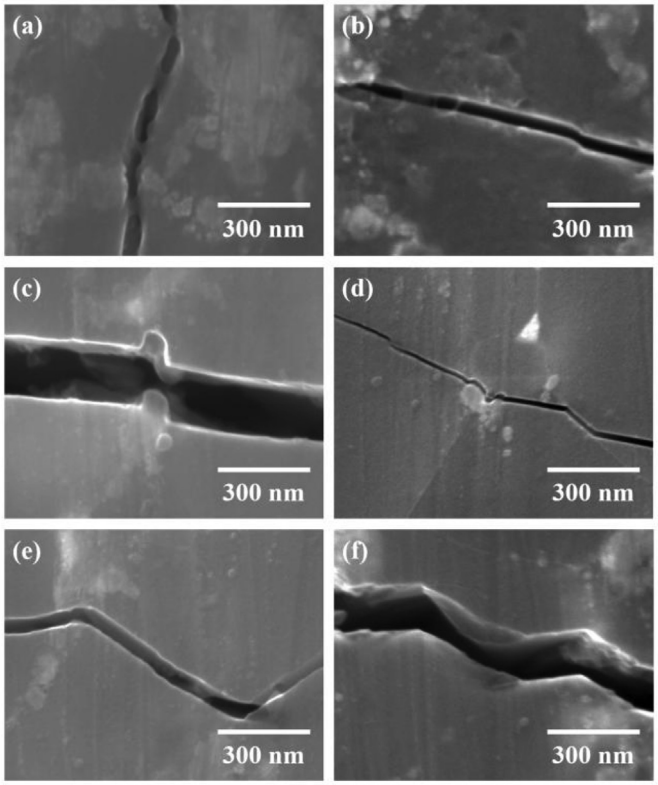

Fig. 2. The three different mechanisms of K_{Ic} enhancement: (a) and (b) bridging of crack, (c) and (d) sheet pullout within the crack, and (e) and (f) deflection of crack propagation in the nanocomposite with 3 vol% rGOs and 0.6 vol% Sn NPs.

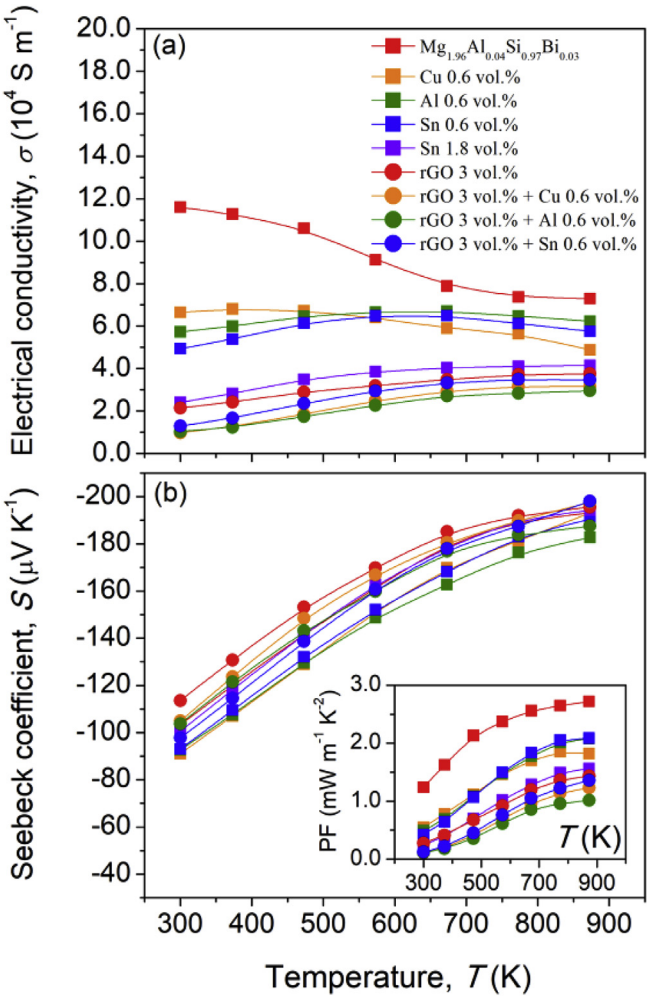

Fig. 3. Temperature dependences of the (a) electrical conductivity and (b) Seebeck coefficient of various nanocomposites. The inset in (b) shows the temperature dependence of the power factor.

are shown for comparison [10,13]. The σ values of $Mg_{1.96}Al_{0.04}Si_{0.97}Bi_{0.03}$ were reduced by the introduction of rGOs and metal NPs. To clarify this, we estimated the n_c and μ_{Hall} values from Hall effect measurement using the one-band model; the results are listed in Table 1. The n_c values of the nanocomposites with dual nanoinclusions (6.15×10^{19} to 7.06×10^{19} cm^{-3}) are lower than those of the metal-NP-embedded nanocomposites (8.96×10^{19} to 9.61×10^{19} cm^{-3}), indicating that the rGOs act as acceptors in an *n*-type Mg_2Si-based matrix. Notably, the μ_{Hall} values significantly decreased by the introduction of the 2D rGOs and 3D metal NPs. Moreover, the formation of an MgO secondary phase (Fig. S2) and a reduction in the grain size (from 3 to 1 μm, Fig. S3), induced by the introduction of the nanoinclusions, caused a reduction in μ_{Hall} [14]. Therefore, the decrease in σ of the nanocomposites was considered to be related to an increase in the electron scattering in the presence of the nanoinclusions, owing to the nanoscale electron mean free path (~20 nm) of the Mg_2Si-based compounds [15,16].

However, the absolute values of *S* were found to be constant or increase slightly by the introduction of rGOs, despite a large decrease in the value of n_c (Table 1). One possible reason for this is the unconventional trade-off between σ and *S* in Mg_2Si-based compounds; the PF value shows an abrupt change with respect to n_c [14,15]. Another reason is the charge compensation effect originated from the hole generation caused by the introduction of *p*-type rGOs. As a result, the PF values of the nanocomposites with dual nanoinclusions (1.02–1.25 mW m^{-1} K^{-2} at 873 K) were much lower than those of the metal-NP-embedded nanocomposites (1.82–2.09 mW m^{-1} K^{-2} at 873 K) and pristine $Mg_{1.96}Al_{0.04}Si_{0.97}Bi_{0.03}$ (2.89 mW m^{-1} K^{-2} at 873 K).

The temperature dependence of κ_{tot} is shown in Fig. 4(a). The κ_{tot} of pristine $Mg_{1.96}Al_{0.04}Si_{0.97}Bi_{0.03}$ was reduced by the introduction of the rGOs and metal NPs for the entire measured temperature range, suggesting a decrease in the phonon relaxation time (τ_I). Nanoinclusions can decrease the lattice thermal conductivity (κ_{lat}) by the effective scattering of mid-frequency phonons according to the equation $\tau_I^{-1} = v(\sigma_s^{-1} + \sigma_I^{-1})^{-1} V_\rho$, where σ_s is the scattering cross-section at the short-wavelength limit, σ_I is the scattering cross-section at the long-wavelength limit, and V_ρ is the number density of the nanoinclusions. To elucidate this phenomenon, we calculated the κ_{lat} values by subtracting the electronic contribution (κ_{ele}) from κ_{tot}. κ_{ele} was estimated using the Wiedemann–Franz law ($\kappa_{ele} = L \cdot \sigma \cdot T$). The L value was approximately 2.44×10^{-8} V^2 K^{-2}. As shown in Fig. 4(b), the metal NPs cannot act as effective phonon scattering centers owing to their intrinsically high κ. Moreover, the κ_{lat} values of the nanocomposites with dual nanoinclusions were much lower than those of the pristine sample at low temperatures, indicating that rGOs were more effective as phonon scattering centers for the Mg_2Si-based compounds compared to the metal NPs. However, the $1/T$ dependence of κ_{lat} was not maintained, owing to an increase in the bipolar contribution (κ_{bp}) from the holes with an increase in the temperature.

Consequently, the TE performance of the nanocomposites with dual nanoinclusions deteriorated, especially at high temperatures, owing to the undesirable effects on the electronic and thermal transport properties originated from the introduction of the rGOs

Table 1
Room temperature electronic transport parameters for the metal nanoparticles embedded nanocomposites with few-layered rGOs.

	σ (S m^{-1})	S (μV K^{-1})	n_c (cm^{-3})	μ_{Hall} (cm^2 V^{-1} s^{-1})
$Mg_{1.96}Al_{0.04}Si_{0.97}Bi_{0.03}$	122596.2	−99.8	9.27×10^{19}	81.4
$Mg_{1.96}Al_{0.04}Si_{0.97}Bi_{0.03}$ + Cu 0.6 vol%	66430.9	−91.1	9.61×10^{19}	42.5
$Mg_{1.96}Al_{0.04}Si_{0.97}Bi_{0.03}$ + Al 0.6 vol%	57326.0	−92.8	8.96×10^{19}	39.3
$Mg_{1.96}Al_{0.04}Si_{0.97}Bi_{0.03}$ + Sn 0.6 vol%	49329.0	−93.0	9.52×10^{19}	31.9
$Mg_{1.96}Al_{0.04}Si_{0.97}Bi_{0.03}$ + Sn 1.8 vol%	24135.2	−100.6	9.30×10^{19}	16.0
$Mg_{1.96}Al_{0.04}Si_{0.97}Bi_{0.03}$ + rGO 3 vol% + Cu 0.6 vol%	10757.7	−98.9	6.15×10^{19}	10.4
$Mg_{1.96}Al_{0.04}Si_{0.97}Bi_{0.03}$ + rGO 3 vol% + Al 0.6 vol%	10392.0	−103.7	6.67×10^{19}	9.6
$Mg_{1.96}Al_{0.04}Si_{0.97}Bi_{0.03}$ + rGO 3 vol% + Sn 0.6 vol%	10415.0	−107.2	7.06×10^{19}	9.1

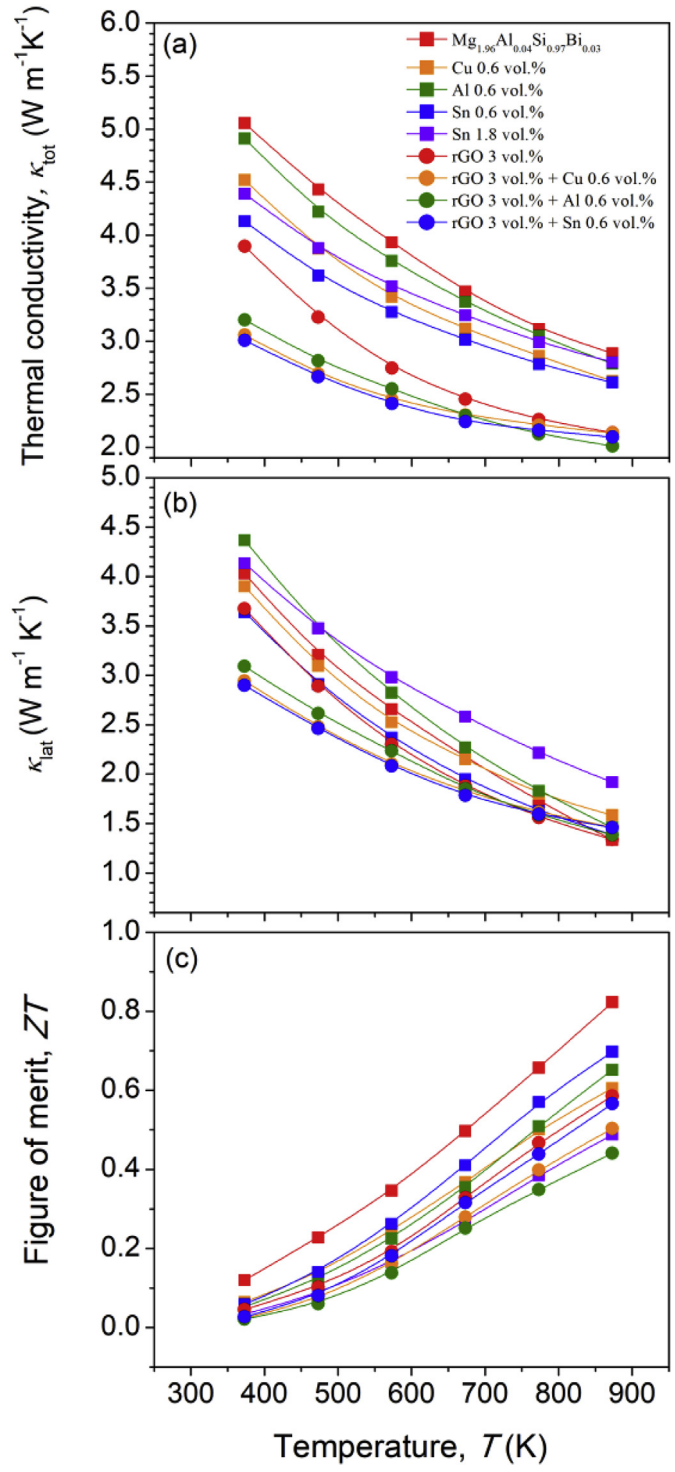

Fig. 4. Temperature dependences of the (a) total thermal conductivity, (b) lattice thermal conductivity, and (c) figure of merit for various nanocomposites.

and metal NPs. Fig. 4(c) presents the ZT values calculated from the measured σ, S, and κ_{tot}. The ZT values (0.44–0.57 at 873 K) of the nanocomposites with dual nanoinclusions were lower than those of pristine $Mg_{1.96}Al_{0.04}Si_{0.97}Bi_{0.03}$ (0.82 at 873 K) and the metal-NP-embedded nanocomposites (0.61–0.70 at 873 K), suggesting a trade-off between mechanical reliability and TE performance for the Mg_2Si-based nanocomposites.

As shown in Fig. 5, the trade-off between K_{Ic} and ZT is an intrinsic drawback of Mg_2Si-based nanocomposites, mainly owing to the similar nanoscale mean free paths (~20 nm) of electrons and phonons [15,16]. However, our results for the variation in K_{Ic} with respect to the TE transport properties of various Mg_2Si-based nanocomposites demonstrate that the trade-off between K_{Ic} and ZT can be improved significantly by preparing nanocomposites with well-designed multiple nanoinclusions. We also determined two critical material design rules to enhance the ZT of Mg_2Si-based TE nanocomposites: (1) compositional tuning of the TE matrix to optimize n_c in order to achieve maximum PF, and (2) selection of nanoinclusions by considering their κ values and bipolar contribution for thermal conduction to achieve minimum $\kappa_{lat} + \kappa_{bp}$.

4. Conclusions

We investigated the effects of multidimensional dual nanoinclusions on the mechanical reliability and TE transport properties of n-type Mg_2Si-based TE compounds. We experimentally demonstrated that the introduction of 2D rGOs and 3D metal NPs was an effective way to enhance the mechanical reliability by intensifying the activation of crack propagation inhibition mechanisms. A significantly enhanced fracture toughness value of ~2.26 MPa m$^{1/2}$ and a moderate ZT value of 0.57 at 873 K were

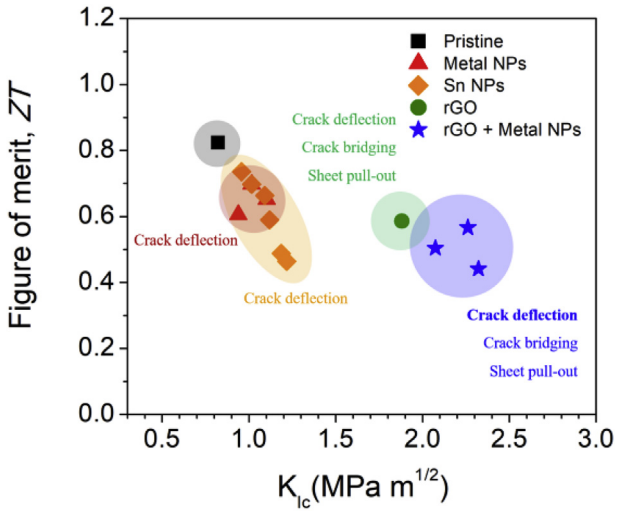

Fig. 5. Dependence of K_{Ic} on the figure of merit for various nanocomposites.

simultaneously obtained for the nanocomposite of $Mg_{1.96}Al_{0.04}Si_{0.97}Bi_{0.03}$ with 3 vol% rGOs and 0.6 vol% Sn NPs; this suggests that our approach of dual nanoinclusions provides an improved trade-off between the mechanical reliability and TE performance of Mg_2Si-based compounds.

Acknowledgements

This work was supported by the National Research Foundation of Korea Grant (2017R1A2A1A17069528) funded by the Korea government (MSIT).

Appendix A. Supplementary data

Supplementary data to this article can be found online at https://doi.org/10.1016/j.jallcom.2019.06.075.

References

[1] K. Koumoto, R. Funahashi, E. Guilmeau, Y. Miyazaki, A. Weidenkaff, Y. Wang, C. Wan, Thermoelectric ceramics for energy harvesting, J. Am. Ceram. Soc. 96 (2013) 1–23.
[2] Z. Li, J.F. Dong, F.H. Sun, S. Hirono, J.F. Li, Significant enhancement of the thermoelectric performance of higher manganese silicide by incorporating MnTe nanophase derived from Te nanowire, Chem. Mater. 29 (2017) 7378–7389.
[3] U.S. Department of Energy (DOE), Thermoelectric Materials, Devices and Systems, Technology Assessment, 2015.
[4] W. Liu, X. Tan, K. Yin, H. Liu, X. Tang, J. Shi, Q. Zhang, C. Uher, Convergence of conduction bands as a means of enhancing thermoelectric performance of n-type $Mg_2Si_{1-x}Sn_x$ solid solutions, Phys. Rev. Lett. 108 (2012) 166601.
[5] Q. Zhang, Y. Zheng, X. Su, K. Yin, X. Tang, C. Uher, Enhanced power factor of $Mg_2Si_{0.3}Sn_{0.7}$ synthesized by a non-equilibrium rapid solidification method, Scripta Mater 96 (2015) 1–4.
[6] P. Nierodaa, J. Leszczynskia, A. Kolezynski, Bismuth doped Mg_2Si with improved homogeneity: synthesis, characterization and optimization of thermoelectric properties, J. Phys. Chem. Solids 103 (2017) 147–159.
[7] G. Kim, J. Kim, H. Lee, S. Cho, I. Lyo, S. Noh, B.W. Kim, S.W. Kim, K.H. Lee, W. Lee, Co-doping of Al and Bi to control the transport properties for improving thermoelectric performance of Mg_2Si, Scripta Mater. 116 (2016) 11–15.
[8] G. Kim, H. Lee, J. Kim, J.W. Roh, I. Lyo, B.W. Kim, K.H. Lee, W. Lee, Up-scaled solid state reaction for synthesis of doped Mg_2Si, Scripta Mater. 128 (2017) 53–56.
[9] Y. Gelbstein, J. Tunbridge, R. Dixon, M.J. Reece, H. Ning, R. Gilchrist, R. Summers, I. Agote, M.A. Lagos, K. Simpson, C. Rouaud, P. Feulner, S. Rivera, R. Torrecillas, M. Husband, J. Crossley, I. Robinson, Physical, mechanical, and structural properties of highly efficient nanostructured n- and p-silicides for practical thermoelectric applications, J. Electron. Mater. 43 (2014) 1703–1711.
[10] G. Kim, H. Lee, J. Kim, J.W. Roh, I. Lyo, B.W. Kim, K.H. Lee, W. Lee, Enhanced fracture toughness of Al and Bi co-doped Mg_2Si by metal nanoparticle decoration, Ceram. Int. 43 (2017) 12979–12982.
[11] G. Kim, S.W. Kim, H.J. Rim, H. Lee, J. Kim, J.W. Roh, B.W. Kim, K.H. Lee, W. Lee, Improved trade-off between thermoelectric performance and mechanical reliability of Mg2Si by hybridization of few-layered reduced graphene oxides, Scripta Mater. 162 (2019) 402–407.
[12] J.J. Kruzic, R.O. Ritchie, Determining the toughness of ceramics from Vickers indentations using the crack-opening displacements: an experimental study, J. Am. Ceram. Soc. 86 (2003) 1433–1436.
[13] G. Kim, H. Lee, H.J. Rim, J. Kim, K. Kim, J.W. Roh, S.M. Choi, B.W. Kim, K.H. Lee, W. Lee, Dependence of mechanical and thermoelectric properties of Mg_2Si-Sn nanocomposites on interface density, J. Alloy. Comp. 769 (2018) 53–58.
[14] J. Boor, T. Dasgupta, H. Kolb, C. Compere, K. Kelm, E. Mueller, Microstructural effects on thermoelectric efficiency: a case study on magnesium silicide, Acta Mater. 77 (2014) 68–75.
[15] N. Satyala, D. Vashaee, Detrimental influence of nanostructuring on the thermoelectric properties of magnesium silicide, J. Appl. Phys. 112 (2012) 093716.
[16] N. Satyala, D. Vashaee, The effect of crystallite size on thermoelectric properties of bulk nanostructured magnesium silicide (Mg_2Si) compounds, Appl. Phys. Lett. 100 (2012) 073107.